

“Blind” Iterative SAFT Reconstruction for Manually Acquired Ultrasonic Measurement Data in Nondestructive Testing

Sayako Koderä

Ilmenau University of Technology
P. O. Box 100565, D-98684 Ilmenau, Germany
Email: sayako.koderä@tu-ilmenau.de

Abstract — There have been developments in nondestructive ultrasonic testing (UT) to assist manual operation for easier and more reliable inspection than conventional ones. Although such system also opens up the possibility to post-process the measurement data for improving imaging quality, manual UT is prone to stochastic observational errors, such as inaccuracy in estimating scan positions or varying coupling, which may cause strong artefacts formation in its reconstruction. In an attempt to reduce the positional-inaccuracy induced artefacts, in this work we propose a preprocessing method to correct the unknown positional error from the measurement data and the erroneous positional information. We demonstrate through simulations that the proposed method is more resistant to positional error and can achieve higher resolution, which is comparable to that of the reconstruction with the exact positional information, than the reconstruction without preprocessing.

Index Terms—Nondestructive testing, Ultrasonic testing, SAFT, Manual measurement, Positional inaccuracy, Total least squares, Newton’s method

I. INTRODUCTION

Ultrasonic testing (UT) is a nondestructive testing method to inspect the structure of test objects without inducing damage. Conventionally, an UT inspection requires either manual operation by a human technician or automated measurement systems. In manual UT, where a human technician observes the change in the echoed pulse, its inspection quality is highly dependent on the expertise of the technician [1]. In automatic UT, on the other hand, measurement data and the corresponding scan positions are recorded, which enables to visualize the inner structure of the test object and further process the data to improve the imaging quality, leading to more reliable inspection quality than its manual counterpart.

Nevertheless, there are still needs for manual UT, for instance when a complex structure is inspected, and its inspection reliability has been of great concern. In order to improve the inspection reliability of manual UT, an assistance system can be employed, which records measurement data and recognizes the scan positions through a tracking system. This

allows us not only to visualize the measurement data but also to process it further to increase its imaging quality [2].

Although their application to manual UT data has been typically excluded, several post-processing techniques have been developed and extensively employed for automatic UT data [3, 4, 5]. While the authors of [3] apply the signal processing methods widely used in the telecommunication field to the UT data, one of the well established post-processing method is the synthetic aperture focusing technique (SAFT) [4, 5]. The aim of SAFT is to improve the spatial resolution through performing superposition with respect to the propagation time delay [6]. In other words, SAFT regards the measurement region-of-interest (ROI) as a synthetic aperture and each measurement as its spatial sampling, indicating that the SAFT reconstruction requires accurate positional information.

On the contrary, the application of such techniques to manual UT data has not been investigated extensively [2, 7]. Previously, we revealed that several stochastic observational errors, such as varying contact pressure or inaccurate positional information due to the tracking error, may result in strong artefacts formation in SAFT reconstructions [8]. Since such errors are inevitable in manual measurement, finding the way to reduce those artefacts could improve the reconstruction quality. Unlike other possible error factors which should be entirely estimated from the measurement data, the tracking error can be handled to some extent, as the positional information is, whether accurate or not, available.

Our goal in this study is to reduce the position-inaccuracy induced artefacts in SAFT reconstructions by correcting the tracking error and modifying the reconstruction system accordingly. Although we are unaware of any other works that deal with this topic, the spatial approximation of the measurement data can be mathematically derived, allowing us to deduce the tracking error by comparing our data model with the actual measurements. This estimate of the tracking error can be utilized to modify the positional information, making it possible to repeat the same procedure to further reduce the tracking error.

Modeling the data, however, requires the information regarding the unknown location of the signal sources. This leads us to formulate a joint optimization problem where both the

position of the signal sources and the tracking error are to be estimated. In order to solve this problem, we introduce two preprocessing steps: firstly the signal source positions are estimated from the measurement data and the erroneous positional information via robust regression technique, and in the next step the tracking error is estimated and corrected iteratively using nonlinear programming. Extensive simulation studies have demonstrated that the proposed method is more resistant to positional error and can achieve higher resolution, which is comparable to that of the reconstruction with the exact positional information, than the reconstruction without preprocessing. Furthermore, the depth-dependency of our method is also investigated, which can be used to determine when it is beneficial to apply error correction.

II. DATA MODEL

For a measurement setup, we consider a manual contact testing where a handheld transducer is placed directly on the specimen surface at a position $\mathbf{p}_k \in \mathbb{R}^3$. The transducer inserts an ultrasonic pulse $h(t)$ into a specimen and receives the reflected signal, A-Scan, at the same position \mathbf{p}_k . The specimen is assumed to be homogenous and isotropic with the constant speed of sound c_0 and to have a flat surface. During the measurement, the contact pressure is considered to be constant so that in the measurement data there is no temporal shift or amplitude change caused by improper coupling. The measurement position \mathbf{p} is arbitrarily selected on the specimen surface and we suppose that there is at least one scatterer inside the specimen, which is regarded as point source.

Conventionally, the inserted pulse $h(t)$ is modeled as a real-valued Gabor function [9], as

$$h(t) = e^{-\alpha t^2} \cdot \cos(2\pi f_C t + \phi), \quad (1)$$

where f_C , α and ϕ are the carrier frequency, the window width factor and the phase, respectively. The time which the sound travels from \mathbf{p}_k to a scatterer \mathbf{s}_i and reflects back to \mathbf{p}_k is so called *time-of-flight*, ToF, which can be obtained with

$$\tau_i(\mathbf{p}_k) = \frac{2}{c_0} \cdot \|\mathbf{s}_i - \mathbf{p}_k\|_2. \quad (2)$$

This includes $\|\mathbf{s}_i - \mathbf{p}_k\|_2$, which is the ℓ_2 norm of the difference between \mathbf{s}_i and \mathbf{p}_k , indicating that the ToF is determined by the position of both measurement and the scatterer.

The obtained A-Scan is the sum of all I reflected echoes, which are delayed version of the inserted pulse $h(t)$

$$a(t; \mathbf{p}_k) = \sum_{i=1}^I \beta_{\mathbf{p}_k, i} \cdot h(t - \tau_i(\mathbf{p}_k)) + n(t), \quad (3)$$

where $\beta_{\mathbf{p}_k, i}$ is the reflection coefficient for the position \mathbf{p}_k and a scatterer \mathbf{s}_i and $n(t)$ is the measurement noise. Since we process the data digitally with the sampling interval of $\text{dt} = \frac{1}{f_s}$, (3) can be formulated as a vector $\mathbf{a}_{\mathbf{p}_k} \in \mathbb{R}^M$ with M representing the number of temporal samples

$$[\mathbf{a}_{\mathbf{p}_k}]_m = \sum_{i=1}^I \beta_{\mathbf{p}_k, i} \cdot h(m \text{ dt} - \tau_i(\mathbf{p}_k)) + [\mathbf{n}]_m. \quad (4)$$

Here $[\cdot]_m$ denotes the m -th element of a vector and $\mathbf{n} \in \mathbb{R}^M$ is the measurement noise in the vector form.

As the specimen is assumed to be isotropic, the ToF changes symmetric with respect to the scatterer \mathbf{s}_i and so does the measurement data. For the sake of simplicity, in this study we consider the case where the measurements are taken along a line on the flat surface, resulting in $\mathbf{p}_k = [x_k \ 0 \ 0]^T$. This indicates that (4) now solely depends on x_k , denoted as \mathbf{a}_k .

By collecting the impulse response at x_k for all possible scatterer positions $\mathbf{s}_i \ \forall i = 1 \dots L$, we can form a measurement dictionary $\mathbf{H}_k \in \mathbb{R}^{M \times L}$ as

$$\mathbf{H}_k = [\mathbf{h}_k^{(1)} \ \mathbf{h}_k^{(2)} \ \dots \ \mathbf{h}_k^{(L)}]. \quad (5)$$

$\mathbf{h}_k^{(l)} \in \mathbb{R}^M$ is the l -th column vector of \mathbf{H}_k , corresponding to the l -th scatterer position in the specimen which is

$$\mathbf{h}_k^{(l)} = \sum_{m=1}^M \beta_{x_k, l} \cdot h(m \text{ dt} - \tau_l(x_k)). \quad (6)$$

This enables us to reformulate (4) as a vector-matrix product as

$$\mathbf{a}_k = \mathbf{H}_k \mathbf{b} + \mathbf{n}, \quad (7)$$

where $\mathbf{b} \in \mathbb{R}^L$ is the vectorized *defect map* which represents the scatterer positions and their amplitudes β_l [10].

After taking K measurements at the positions $\mathbf{x} \in \mathbb{R}^K$, we can obtain the set of measurements $\mathbf{A} \in \mathbb{R}^{M \times K}$ as

$$\mathbf{A} = [\mathbf{a}_1 \mathbf{a}_2 \dots \mathbf{a}_L]. \quad (8)$$

Column-wise concatenation of measurement dictionaries for all scan positions yields the complete dictionary $\mathbf{H} \in \mathbb{R}^{MK \times L}$

$$\mathbf{H} = \begin{bmatrix} \mathbf{H}_1 \\ \mathbf{H}_2 \\ \vdots \\ \mathbf{H}_K \end{bmatrix}. \quad (9)$$

This allows us to express \mathbf{A} as linear transform similar to (7)

$$\text{vec}\{\mathbf{A}\} = \mathbf{H} \mathbf{b} + \text{vec}\{\mathbf{N}\}, \quad (10)$$

in which $\text{vec}\{\cdot\}$ is the vectorize operation of a matrix and $\text{vec}\{\mathbf{N}\} \in \mathbb{R}^{MK}$ is the concatenation of all noise vectors.

The ultimate goal of the inspection is to locate the scatterer positions, which can be recovered from (10) with SAFT by computing

$$\hat{\mathbf{b}} = \mathbf{H}^T \text{vec}\{\mathbf{A}\}. \quad (11)$$

III. EMPLOYED OPTIMIZATION TECHNIQUES

In the proposed method of this study, two different optimization techniques are used, namely the total least-squares (TLS) and the Newton's method. The former is employed to estimate the scatterer positions, whereas the latter is applied to correct the tracking error based on the estimated scatterer positions. In this section, the basic ideas and approaches of those techniques are presented.

A. Total Least-Squares

The TLS method seeks for an optimal solution of an overdetermined system of equations

$$\Omega \approx \Psi \Upsilon \quad (12)$$

where $\Omega \in \mathbb{C}^{m \times d}$ and $\Psi \in \mathbb{C}^{m \times n}$ are the given data and $\Upsilon \in \mathbb{C}^{n \times d}$ is unknown with $n, d < m$ [11].

With $m > n$ and Ψ being full column rank, there is typically no exact solution, requiring Υ to be approximated. Unlike the least-squares approach, where all modeling errors are assumed to be originated from the dependent variables Ω , TLS takes into account the errors in both Ω and Ψ . By incorporating the errors on both sides, the approximation (12) becomes an equality

$$\Omega + \Delta\Omega = (\Psi + \Delta\Psi) \Upsilon, \quad (13)$$

with $\Delta\Omega \in \mathbb{C}^{m \times d}$ and $\Delta\Psi \in \mathbb{C}^{m \times n}$ representing the introduced perturbations on both sides. Under the assumption that $\Delta\Omega$ and $\Delta\Psi$ are independent, TLS seeks for the solution which minimizes both perturbations while satisfying the perturbed equation (13) [11]

$$\min \|\begin{bmatrix} \Delta\Psi & \Delta\Omega \end{bmatrix}\|_F^2 \quad \text{s.t.} \quad \Omega + \Delta\Omega = (\Psi + \Delta\Psi) \Upsilon. \quad (14)$$

In order to solve (14), singular value decomposition (SVD) can be utilized [11, 12]. Without perturbations Ψ and Ω are assumed to be linearly independent, making their concatenation matrix full column-rank of $n + d$. The SVD of this concatenation matrix can be obtained as

$$\begin{aligned} \begin{bmatrix} \Psi & \Omega \end{bmatrix} &= U \Sigma V^H \\ &= \begin{bmatrix} U_1 & U_2 \end{bmatrix} \begin{bmatrix} \Sigma_1 & \mathbf{0}_{n \times d} \\ \mathbf{0}_{(m-n) \times n} & \Sigma_2 \end{bmatrix} \begin{bmatrix} V_{11} & V_{12} \\ V_{21} & V_{22} \end{bmatrix}^H, \end{aligned} \quad (15)$$

where $U \in \mathbb{C}^{m \times m}$ and $V \in \mathbb{C}^{(n+d) \times (n+d)}$ are both unitary matrices and orthogonal to each other, whereas $\Sigma \in \mathbb{R}_+^{m \times (n+d)}$ is a diagonal matrix containing $n + d$ singular values. U , Σ and V are further divided into sub matrices $U_1 \in \mathbb{C}^{m \times n}$ and $U_2 \in \mathbb{C}^{m \times (m-n)}$, $\Sigma_1 \in \mathbb{R}_+^{n \times n}$ and $\Sigma_2 \in \mathbb{R}_+^{(m-n) \times d}$ and $V_{11} \in \mathbb{C}^{n \times n}$, $V_{12} \in \mathbb{C}^{n \times d}$, $V_{21} \in \mathbb{C}^{d \times n}$ and $V_{22} \in \mathbb{C}^{d \times d}$, respectively.

The perturbed equation (13) indicates that the perturbed matrices span the same subspace, i.e. $\text{col}\{\Omega + \Delta\Omega\} = \text{col}\{\Psi + \Delta\Psi\}$ with $\text{col}\{\cdot\}$ representing the column space of a matrix. This results in the concatenation matrix of perturbed matrices with the rank of n , whose SVD can be expressed as

$$\begin{bmatrix} \Psi + \Delta\Psi & \Omega + \Delta\Omega \end{bmatrix} = U_1 \Sigma_1 \begin{bmatrix} V_{11}^H & V_{21}^H \end{bmatrix}. \quad (16)$$

With this concatenation matrix, the perturbed equation (13), which is the constraint of the cost function (14), can be formulated as

$$\begin{bmatrix} \Psi + \Delta\Psi & \Omega + \Delta\Omega \end{bmatrix} \begin{bmatrix} \Upsilon \\ -I_d \end{bmatrix} = \mathbf{0}_{m \times d}. \quad (17)$$

This suggests that $\begin{bmatrix} \Upsilon^H & -I_d \end{bmatrix}$ lies in the nullspace of the concatenation of the perturbed matrix

$\text{null}\{\begin{bmatrix} \Psi + \Delta\Psi & \Omega + \Delta\Omega \end{bmatrix}\}$, which is equal to $\text{null}\{\begin{bmatrix} V_{11}^H & V_{21}^H \end{bmatrix}\}$. Hence, $\begin{bmatrix} \Upsilon^H & -I_d \end{bmatrix}$ spans the same subspace as $\begin{bmatrix} V_{12}^H & V_{22}^H \end{bmatrix}$, leading to the TLS solution for (14)

$$\Upsilon_{\text{TLS}} = -V_{12} V_{22}^{-1}. \quad (18)$$

B. Newton's Method

In optimization, the Newton's method is applied to solve unconstrained nonlinear optimization problems iteratively using both first and second derivative of the cost function. Despite its fast convergence, the Newton's method is often less preferred to other gradient-based methods, such as quasi-Newton's method, since it requires to compute the second derivative, which is computationally expensive. Yet, if the second derivative for the particular problem is easy to calculate, it provides more precise and faster convergence than its counterparts which rely only on the first derivative [13].

Suppose we want to minimize a twice differentiable cost function $f: \mathbb{R}^L \rightarrow \mathbb{R}$

$$\min_{x \in \mathbb{R}^L} f(x). \quad (19)$$

The solution of this problem x_{opt} should satisfy the following two necessary conditions [14]:

$$\text{NC1: } \nabla f(x_{\text{opt}}) = g(x_{\text{opt}}) = \mathbf{0}_L$$

$$\text{NC2: } \frac{\partial^2 f(\hat{x}_{\text{opt}})}{\partial x_i \partial x_j} = \mathbf{H}_f(\hat{x}_{\text{opt}}) \succeq 0 \quad (\text{positive semi-definite}).$$

Under the assumption that NC2 is satisfied for all $x \in \mathbb{R}^L$, the Newton's method converges towards x_{opt} by seeking for the roots of g , which is equivalent to NC1.

Each iteration of the Newton's method computes a search direction d_n based on the current iterate x_n and searches for a new iterate x_{n+1} whose function value $f(x_{n+1})$ is lower than the current one $f(x_n)$ [13]. Both the function value and its gradient of the next iterate can be expressed with the current iterate using Taylor expansion as

$$\begin{aligned} f(x_{n+1}) &= f(x_n + d_n) \\ &\approx f(x_n) + [g(x_n)]^T d_n + \frac{1}{2} d_n^T \mathbf{H}_f(x_n) d_n \end{aligned} \quad (20)$$

$$g(x_{n+1}) = g(x_n + d_n) \approx g(x_n) + \mathbf{H}_f(x_n) d_n. \quad (21)$$

Considering (21) to satisfy NC1 yields the search direction as

$$d_n = -[\mathbf{H}_f(x_n)]^{-1} [g(x_n)]^T, \quad (22)$$

which can be inserted into (20)

$$f(x_{n+1}) \approx f(x_n) - \frac{1}{2} [g(x_n)]^T [\mathbf{H}_f(x_n)]^{-1} g(x_n). \quad (23)$$

Since \mathbf{H}_f is assumed to be positive semi-definite, $f(x_{n+1}) \leq f(x_n)$ is ensured, suggesting that d_n in (22) is an appropriate choice for the search direction.

IV. BLIND ERROR CORRECTION (BEC)

Although SAFT reconstruction is well known for its robustness, computing the measurement matrix from the inaccurate positional information may significantly impair the imaging quality of its reconstruction. However, if the deviation between the actual and the tracked positions is little, the measurement matrix for the actual positions can be spatially approximated via the first order Taylor approximation which we discussed in Section III.B. The same analogy can be employed for approximating the measurement matrix \mathbf{H} in (10).

In this study, we suppose that K measurements are taken at the positions $\mathbf{x} \in \mathbb{R}^K$ which are recognized falsely by the tracking system with the tracking error $\Delta\mathbf{x} \in \mathbb{R}^K$. This leads the measurement assistance system to provide us the inaccurate positional information $\hat{\mathbf{x}} = \mathbf{x} + \Delta\mathbf{x}$. Based on the available information, namely the measurement data \mathbf{A} and the tracked positions $\hat{\mathbf{x}}$, we aim to estimate and correct the tracking error through comparing our data model with the actual measurement data.

For a single A-Scan taken at x_k , the measurement matrix of the actual position can be approximated with its tracked position \hat{x}_k and deviation Δx_k as

$$\mathbf{H}_k \approx \hat{\mathbf{H}}_k - \hat{\mathbf{J}}_k \cdot \Delta x_k. \quad (24)$$

Here, $\mathbf{H}_k \in \mathbb{R}^{M \times L}$ and $\hat{\mathbf{H}}_k \in \mathbb{R}^{M \times L}$ are the measurement matrix at the actual position x_k and the tracked position \hat{x}_k , respectively, while $\hat{\mathbf{J}}_k \in \mathbb{R}^{M \times L}$ denotes the derivative of the measurement matrix with respect to the position at \hat{x}_k . The derivative of the measurement matrix is obtained from

$$\hat{\mathbf{J}}_k = \begin{bmatrix} \hat{j}_k^{(1)} & \hat{j}_k^{(2)} & \cdots & \hat{j}_k^{(L)} \end{bmatrix}, \quad (25)$$

where its column vectors are derived from the corresponding column vectors of the measurement matrix with

$$\hat{j}_k^{(l)} = \frac{\partial \hat{h}_k^{(l)}}{\partial x}. \quad (26)$$

The approximation of the complete measurement matrix \mathbf{H} of the actual measurement positions \mathbf{x} can be now expressed based on (9) and (24) as

$$\begin{aligned} \mathbf{H} &\approx \begin{bmatrix} \hat{\mathbf{H}}_1 \\ \hat{\mathbf{H}}_2 \\ \vdots \\ \hat{\mathbf{H}}_K \end{bmatrix} - \begin{bmatrix} \hat{\mathbf{J}}_1 \cdot \Delta x_1 \\ \hat{\mathbf{J}}_2 \cdot \Delta x_2 \\ \vdots \\ \hat{\mathbf{J}}_K \cdot \Delta x_K \end{bmatrix} \\ &= \hat{\mathbf{H}} - \mathbf{E}\hat{\mathbf{J}}. \end{aligned} \quad (27)$$

Here, $\hat{\mathbf{J}} \in \mathbb{R}^{MK \times L}$ is the complete derivative matrix, whereas $\mathbf{E} \in \mathbb{R}^{MK \times MK}$ is obtained from

$$\mathbf{E} = \text{diag}\{\Delta\mathbf{x}\} \otimes \mathbf{I}_M \quad (28)$$

with the diagonalization operator $\text{diag}\{\cdot\}$ and \otimes representing the Kronecker product.

Based on (10) and (27), the measurement data can be modeled as

$$\text{vec}\{\mathbf{A}\} \approx [\hat{\mathbf{H}} - \mathbf{E}\hat{\mathbf{J}}] \mathbf{b} + \text{vec}\{\mathbf{N}\}. \quad (29)$$

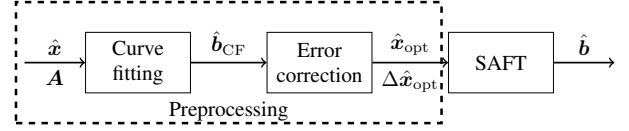


Figure 1: Block diagram of the blind error correction as preprocessing

Yet, for estimating the tracking error we still lack the information regarding the scatterer positions \mathbf{b} , resulting in (29) becoming a joint optimization problem as

$$\min_{\Delta\mathbf{x}} \min_{\mathbf{b}} \left\| \text{vec}\{\mathbf{A}\} - [\hat{\mathbf{H}} - \mathbf{E}\hat{\mathbf{J}}] \mathbf{b} \right\|_2^2. \quad (30)$$

Solving (30) can be divided into two steps shown as Fig. 1. Firstly we estimate the scatterer positions \mathbf{b} via curve fitting while taking the tracking error into account. Then, we aim to estimate and correct the tracking error iteratively by comparing our data model in (29) to the measurement data. In the following subsections we demonstrate each step of the preprocessing in detail.

A. TLS Curve Fitting

The goal of this preprocessing step is to estimate the scatterer positions based on which we can model the measurement data in the next step. Here we assume that the total of I scatterers are located sufficiently far apart in the specimen so that they can be separated into single source from the measurement data. Thus, we aim to estimate the scan position of a single scatter $\mathbf{s}_i = \begin{bmatrix} x_i^{(s)} & z_i^{(s)} \end{bmatrix}$, which resides in the ROI, from the measurement data corresponding to this particular region \mathbf{a}^{ROI} and the erroneous positional information $\hat{\mathbf{x}}$.

What we know regarding the measurement data is its geometric properties. Due to the symmetric change in the ToF with respect to the scatterer \mathbf{s}_i , the collection of the measurements, called B-Scan, follows a similar trend as hyperbola. Although they are not the same, a hyperbola can be, with the proper parameterization, well approximated as a parabola within a limited horizontal range. The horizontal range of the UT measurement data is typically very limited as it is confined to the beam spread of the transducer. This enables us to approximate the curve, which a set of measurement data traces, as a parabola, providing the information on the scatterer position.

One approach to find the best approximate is curve fitting. In the sense of a parabola this can be done via quadratic regression, where we seek to fit the data to a quadratic equation. For the measurement data $\mathbf{a}_k^{\text{ROI}}$ taken at the position x_k , the polynomial model of the data can be expressed as

$$z_k = w_0 + w_1 \cdot x_k + w_2 \cdot x_k^2, \quad (31)$$

where z_k denotes the peak position of $\mathbf{a}_k^{\text{ROI}}$ and w_0 , w_1 and w_2 are polynomial coefficients. From these coefficients, the scatterer positions can be calculated with

$$x_i^{(s)} = -\frac{w_1}{2w_2}, \quad z_i^{(s)} = w_0 - \frac{w_1^2}{4w_2}. \quad (32)$$

Since there are three unknowns in the polynomial, more than three A-Scans are required, and to achieve the sufficient precision of the model the total number of $K \gg 3$ A-scans are considered to be collected at the scan positions $\mathbf{x} \in \mathbb{R}^K$. This lets us formulate (32) as a vector-matrix product as

$$\begin{bmatrix} z_1 \\ z_2 \\ \vdots \\ z_K \end{bmatrix} = \begin{bmatrix} 1 & x_1 & x_1^2 \\ 1 & x_2 & x_2^2 \\ \vdots & \vdots & \vdots \\ 1 & x_K & x_K^2 \end{bmatrix} \begin{bmatrix} w_0 \\ w_1 \\ w_2 \end{bmatrix}, \quad (33)$$

which can be simply denoted as $\mathbf{z} = \mathbf{X}\mathbf{w}$ with $\mathbf{z} \in \mathbb{R}^K$, $\mathbf{X} \in \mathbb{R}^{K \times 3}$ and $\mathbf{w} \in \mathbb{R}^3$.

The problem here is that both dependent and independent variables, \mathbf{z} and \mathbf{X} respectively, contain the error. \mathbf{z} may include the measurement noise, quantization error or other possible errors, whereas \mathbf{X} is corrupted due to the tracking error. This results in (33) becoming approximation which can be solved via TLS as these errors are independent. Hence, we can estimate the position of \mathbf{s}_i by solving the following optimization problem

$$\min \|\begin{bmatrix} \Delta \mathbf{z} & \Delta \mathbf{X} \end{bmatrix}\|_{\text{F}}^2 \quad \text{s.t.} \quad \mathbf{z} + \Delta \mathbf{z} = (\mathbf{X} + \Delta \mathbf{X})\mathbf{w}. \quad (34)$$

B. Iterative Error Correction

In the second step of the preprocessing, the tracking error should be estimated and corrected. As the scatterer positions are estimated in the prior process, yielding $\hat{\mathbf{b}}_{\text{CF}}$, measurement data can be modeled with (29) based on the tracked positions $\hat{\mathbf{x}}$ and $\hat{\mathbf{b}}_{\text{CF}}$. We now can formulate an optimization problem to estimate the tracking error as

$$\min_{\Delta \mathbf{x}} f(\Delta \mathbf{x}) = \left\| \text{vec}\{\mathbf{A}\} - \hat{\mathbf{H}}\hat{\mathbf{b}}_{\text{CF}} + \mathbf{E}\hat{\mathbf{J}}\Delta \mathbf{x} \right\|_2^2. \quad (35)$$

As (35) is an unconstrained nonlinear problem, it can be solved iteratively using, for instance, the Newton's method.

Employing the Newton's method is, however, only meaningful, when the Hessian matrix of (35) is proven to be easy to compute. Considering that all $\text{vec}\{\mathbf{A}\}$, $\hat{\mathbf{H}}\hat{\mathbf{b}}_{\text{CF}}$ and $\hat{\mathbf{J}}\hat{\mathbf{b}}_{\text{CF}}$ are vectors, $f(\Delta \mathbf{x})$ in (35) can be simplified as

$$f(\Delta \mathbf{x}) = \left\| \tilde{\boldsymbol{\alpha}} + \mathbf{E}\tilde{\mathbf{j}} \right\|_2^2 = \left[\tilde{\boldsymbol{\alpha}} + \mathbf{E}\tilde{\mathbf{j}} \right]^T \left[\tilde{\boldsymbol{\alpha}} + \mathbf{E}\tilde{\mathbf{j}} \right]. \quad (36)$$

$\tilde{\boldsymbol{\alpha}} \in \mathbb{R}^{MK}$ represents the difference of the $\text{vec}\{\mathbf{A}\}$ and $\hat{\mathbf{H}}\hat{\mathbf{b}}_{\text{CF}}$, while $\tilde{\mathbf{j}} \in \mathbb{R}^{MK}$ denotes the vector obtained from $\hat{\mathbf{J}}\hat{\mathbf{b}}_{\text{CF}}$, both of which are concatenation of M length vector related to a single A-Scan and the corresponding data model of each measurement position

$$\tilde{\boldsymbol{\alpha}} = \begin{bmatrix} \boldsymbol{\alpha}_1 \\ \boldsymbol{\alpha}_2 \\ \vdots \\ \boldsymbol{\alpha}_K \end{bmatrix}, \quad \tilde{\mathbf{j}} = \begin{bmatrix} \mathbf{j}_1 \\ \mathbf{j}_2 \\ \vdots \\ \mathbf{j}_K \end{bmatrix}. \quad (37)$$

Since \mathbf{E} is a diagonal matrix, indicating that the tracking error of each measurement position only accounts for the

corresponding modeled A-Scan, the gradient and the Hessian matrix of f can be calculated very easily with

$$g(\Delta \mathbf{x}) = \begin{bmatrix} 2 \cdot \boldsymbol{\alpha}_1^T \mathbf{j}_1 + \Delta x_1 \cdot \|\mathbf{j}_1\|_2^2 \\ 2 \cdot \boldsymbol{\alpha}_2^T \mathbf{j}_2 + \Delta x_2 \cdot \|\mathbf{j}_2\|_2^2 \\ \vdots \\ 2 \cdot \boldsymbol{\alpha}_K^T \mathbf{j}_K + \Delta x_K \cdot \|\mathbf{j}_K\|_2^2 \end{bmatrix}, \quad (38)$$

and

$$\mathbf{H}_f(\Delta \mathbf{x}) = \text{diag}\{\|\mathbf{j}_k\|_2^2\}_{k=1}^K. \quad (39)$$

This implies that we can benefit from the fast convergence of the Newton's method without expensive calculation of the second derivative.

After we estimate the deviation $\Delta \hat{\mathbf{x}}$ by solving (35) via the Newton's method, we modify the erroneous positional information $\hat{\mathbf{x}}$ to $\hat{\mathbf{x}} = \hat{\mathbf{x}} - \Delta \hat{\mathbf{x}}$ and repeat the same procedure based on the newly set and improved positional information $\hat{\mathbf{x}}$. As a result, the deviation to the actual measurement positions is reduced with each iteration, improving the accuracy of the measurement matrix in (27) which is used for the reconstruction in (11).

V. SIMULATION: INVESTIGATION OF ERROR TOLERANCE AND IMPACT ANALYSIS OF THE ROI DEPTH

Performance of the proposed method was examined through two simulation studies: the simulation I shows the error sensitivity of the proposed method, while the simulation II illustrates the impact of the ROI depth. The former seeks to provide the insight to assess whether the proposed method is appropriate for the selected measurement assistance system whose error deviation is known as a part of the device specifications. The simulation II, on the other hand, is aimed to determine from and up to which ROI depth it is worthwhile to correct the error, since the impact of the horizontal deviation varies with the ROI depth.

A. Assumptions and Test Parameters

We conducted sets of Monte Carlo simulations with respect to the tracking error with an aluminum object for which we set the same assumptions as we described in Sec. II. For the sake of simplicity, the measurement data is regarded as noise free. Our ROI contains one scatterer and is a part of the test object where back and side wall echoes can be neglected. The transducer parameters we assumed are based on the Olympus standard contact transducer SUC 166-1 [15].

Each measurement data is considered to be taken at a measurement grid point. The resolution of the tracking system, on the other hand, depends on the camera specifications and is assumed to be finer than the measurement grids in order to minimize the quantization error. This means that the tracking positions may be between two grid points, based on which the corresponding measurement matrix is calculated. Since more than three A-Scans are required to estimate a scatterer position, we consider an offline reconstruction process, where each measurement data is first stored in the system before it is reconstructed together with the other A-Scans. Table I provides a summary of the test parameters.

Simulation	Parameter	Value
For both simulations	Dimension (L × H)	40 mm × 100 mm
	Speed of sound c_0	6300 m s ⁻¹
	Sampling frequency f_S	80 MHz
	Transducer element frequency f_C	5 MHz
	Transducer element diameter	4.75 mm
	Transducer beam spread	30°
	Wavelength λ	1.6 mm
	Bandwidth factor α	20 (mm/s) ²
	Reflection coefficient β	1
	Horizontal sampling interval dx	0.5 mm
	Vertical sampling interval dz	39.375 μ m
	Scatterer position s_x	20 mm
Simulation I	Number of realizations	200
	Error distribution	uniform
Simulation II	Scatterer position s_z	20 ... 50 mm
	Tracking error	0.1 ... 1 λ

Table I: Summary of the test parameter values for the simulations

B. Evaluation Metrics

Since the imaging quality is strongly related to the human perception, providing satisfactory numerical evaluations is challenging. For this reason, we used three different metrics: normalized root squared error SE^\dagger , *Array Performance Indicator* (API) [16] and *Generalized Contrast-to-Noise Ratio* (gCNR) [17]. As reference we chose the reconstruction results of the measurement data which is processed at the exact measurement positions.

The normalized root squared error SE^\dagger shows the difference between the obtained reconstruction results $\hat{\mathbf{B}}$ and the reference \mathbf{B} . This is calculated with

$$SE^\dagger = \frac{\|\gamma \hat{\mathbf{B}} - \mathbf{B}\|_2}{\|\mathbf{B}\|_2}, \quad (40)$$

where γ is a normalization factor which can be obtained from

$$\gamma = \frac{\text{vec}\{\mathbf{B}\}^T \text{vec}\{\hat{\mathbf{B}}\}}{\text{vec}\{\hat{\mathbf{B}}\}^T \text{vec}\{\hat{\mathbf{B}}\}}. \quad (41)$$

The API evaluates the reconstruction resolution in terms of the area which is above a certain threshold, suggesting that the better resolution is attainable with the smaller API. This is defined by [16]

$$API = \frac{A_\epsilon}{\lambda^2}, \quad (42)$$

where A_ϵ and λ denote the area which is above the given threshold ϵ and the wavelength, respectively. In this study we considered the envelop of the reconstruction image and set ϵ to -3 dB of its maximum value.

On the other hand, the gCNR accounts more for human perception of the image contrast by considering the overlap of the probability density functions of inside and outside the target area [17]. For the given target area, the overlap of the probability density functions is calculated with

$$OVL = \int \min\{p_i(x), p_o(x)\} dx, \quad (43)$$

where OVL represents the overlap, while p_i and p_o are the probability density function of inside and outside the target area, respectively. Based on this, the gCNR is obtained from

$$gCNR = 1 - OVL, \quad (44)$$

revealing that the higher gCNR value indicates the better resolution of the image. Here we defined the target area from the reference where its envelope is above -3 dB of its maximum value.

Since we conducted sets of Monte Carlo simulations, the average value of each data set, denoted as MSE^\dagger , MAPI and MgCNR, is calculated and shown in the following sections.

C. Results of the Simulation I

Figure 2 presents the evaluation of the obtained results for the simulation I, and Figure 3, 5b, 5e and 5h show the corresponding example reconstruction images. We compared three results: reconstruction without error correction, with error correction (BEC) and the reference.

If the tracking error is very little, up to 0.4λ in the selected ROI, MAPI and MgCNR of the uncorrected reconstruction remains almost the same, showing that such error has negligible effect on the imaging quality. Although it is within the satisfying level, MSE^\dagger and MgCNR of the proposed method is worse than that of the uncorrected one. At the same time, MAPI remains low, which suggests that for a small range of the error approximating the measurement matrix causes weak but more artefacts in the reconstruction than an erroneous measurement matrix. Correcting the tracking error for this error range is, thus, not necessary.

With increasing error, all results illustrate that the tracking error starts making nonnegligible difference between the erroneous and the actual measurement matrices and affecting the imaging quality of the reconstructions. Despite their similar MgCNR values, the MAPI values of the uncorrected and the corrected reconstruction vary significantly. These results imply that, while both reconstruction contains the same "amount" of the artefacts, the magnitude of the artefacts in the uncorrected reconstruction is stronger than that in the error-corrected counterpart. Indeed, the imaging quality of the proposed method is comparable to that of the reference (Figure 5h and 5b). This indicates that the proposed method can tolerate larger positional error than reconstructing without preprocessing.

D. Results of the Simulation II

The evaluation of the simulation II is presented in Figure 4, and the example reconstruction results are provided in Figure 5. Both results demonstrate that the ROI depth affects the performance of the proposed method.

Near the object surface, in our case up to 20 mm depth, the imaging quality of the SAFT reconstruction, including the reference, is degraded than the deeper region. This is firstly because of the limited horizontal range due to the transducer beam spread, which generally impairs the spatial resolution of SAFT reconstructions. Furthermore, there is larger change in the ToF of two consecutive scan positions than the deeper

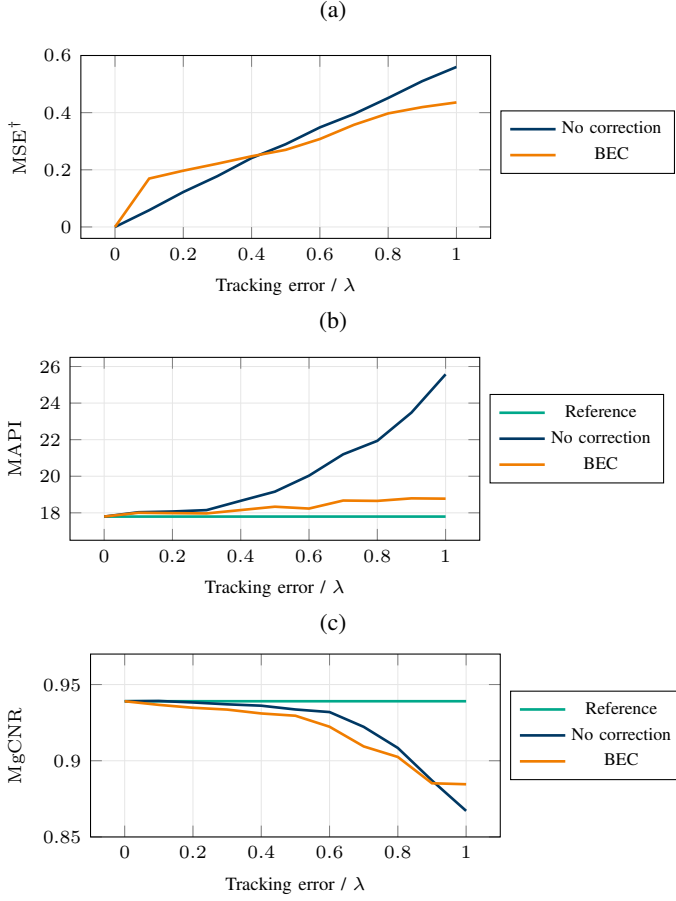


Figure 2: Results obtained with the simulation I: the reconstruction imaging quality for the varying tracking error

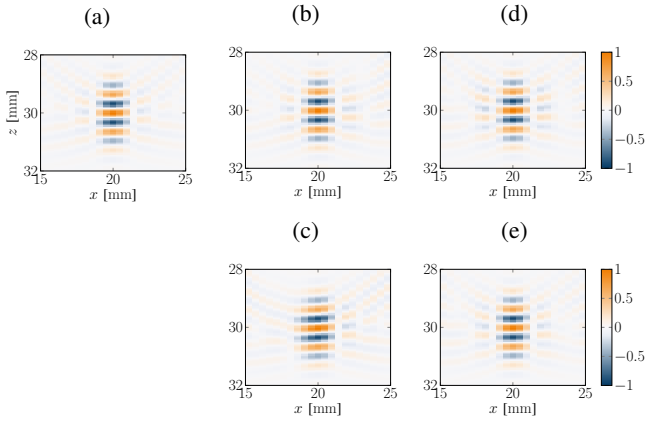


Figure 3: Example reconstruction results of the simulation I: 3a for reference reconstruction, 3b and 3c for reconstruction without correction and 3d and 3e for reconstruction with BEC. The upper row (except the reference) is with the tracking error of 0.4λ , while the lower row is with the error of 0.8λ .

region. This not only causes the same horizontal deviation to have more impact on the imaging quality than the deeper region but also reduces the validity range of the spatial approximation. Consequently, the proposed method becomes very susceptible to the horizontal deviation and yields similar or even worse results compared to the reconstruction without error correction.

If the ROI lies deeper in the object, the resolution of all SAFT reconstructions becomes better than in the shallower region. This is because the horizontal range captured within the beam spread expands, enhancing the SAFT reconstruction, which can be seen in improved value of MAPI and MgCNR in the reference. The most significant improvement in the imaging quality, however, can be observed in our proposed method. As Figure 5h demonstrates, artefacts formation is considerably reduced, resulting in the improved evaluation values in Figure 4. This is due to the fact that there is smaller change in ToF between two neighboring scans than in the shallower region, which increases the validity range of the spatial approximation and enables to correct the tracking error. Decrease in the ToF change also makes the horizontal deviation less impactful compared to the near surface region, however the uncorrected reconstruction shows less significant improvement than our proposed method, revealing that either strong artefacts or horizontal shifts in the reconstruction cannot be avoided in this region (Figure 5e). Overall, the results suggest that applying error correction is beneficial, if the ROI does not lie near the surface.

In much deeper region, deeper than 50 mm for our setup, the evaluation results in Figure 4 indicates that the resolution of all three methods converges. Notably, MgCNR of the proposed method converges to that of the reference, demonstrating that in this region the tracking error can be very well corrected. Even without error correction, a satisfying resolution is attainable (Figure 5f). This implies that the horizontal deviation of 1λ has little effect on the imaging quality in this region. Although applying error correction may seem not worthwhile, both MAPI and MgCNR show that the uncorrected reconstruction cannot achieve the high resolution as that of other two reconstructions. This may become crucial for reconstructing the actual measurement data, as the attainable resolution is much lower than that of the simulations based on the point source assumption.

VI. CONCLUSION

In this study we presented a two-step preprocessing method to reduce position-inaccuracy induced artefacts in SAFT reconstructions through correcting the unknown positional error. Since the errors in the available information are independent, we devised the first part of the preprocessing as a TLS polynomial regression problem to estimate the scatterer positions. The second part is formulated as a nonlinear optimization problem to estimate and correct the tracking error, which can be solved via Newton's method as its Hessian matrix is very easy to compute. Simulation studies have demonstrated that the proposed method can tolerate larger error and achieve higher resolution

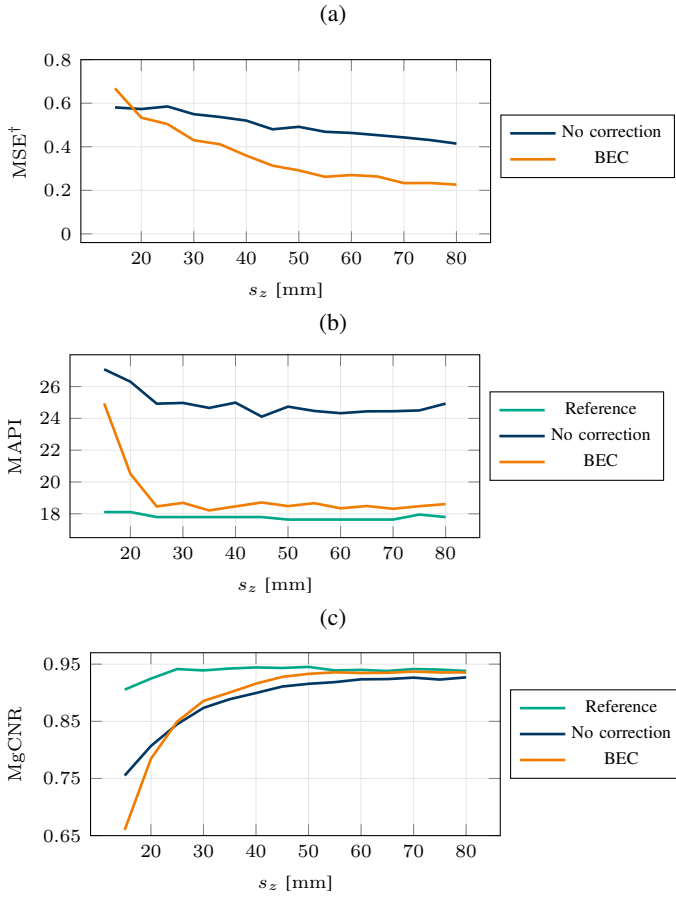


Figure 4: Results obtained with the simulation II: the reconstruction imaging quality for the varying ROI depth

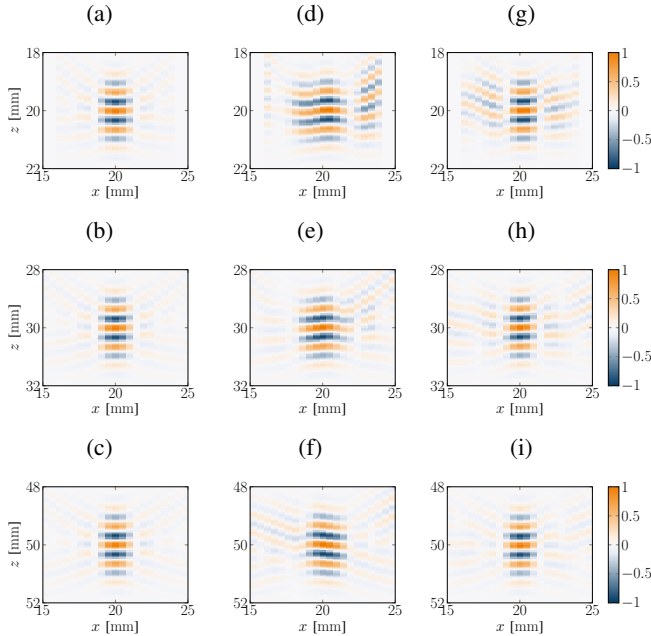


Figure 5: Example reconstruction results of the simulation II: 5a to 5c for reference reconstruction, 5d to 5f for reconstruction without correction and 5g to 5i for reconstruction with BEC

than reconstructing without preprocessing. Considering the physical size of the signal source in actual measurements, which alone impairs the resolution of SAFT reconstructions, our method has the potential to greatly reduce error-induced artefacts and realize previously unreachable imaging quality for manual inspection.

REFERENCES

- [1] P. Cawley. Non-destructive testing - current capabilities and future directions. *Proceedings of the Institution of Mechanical Engineers, Part L*, vol 215, 2001.
- [2] F. Krieg, S. Lugin, J. Kirchhof, A. Ihlow, T. Schwender, G. del Galdo, F. Römer, and A. Osman. Saft processing for manually acquired ultrasonic measurement data with 3D smartinspect. 2018. SHM-NDT.
- [3] L. Ericsson and M.G. Gustafsson. Perception and Entropy Inspired Ultrasonic Grain Noise Suppression using Noncoherent Detector Statistics. In *ECNDT*, 1998.
- [4] T.E. Hall, L.D. Reid, and S.R. Doctor. The SAFT-UT Real-Time Inspection System - Operational Principles and Implementation. Technical report, Pacific Northwest Laboratory, 1988.
- [5] J. Krautkrämer and H. Krautkrämer. *Ultrasonic Testing of Materials*. Springer-Verlag, 1990.
- [6] F. Lingvall. *Time-domain Reconstruction Methods for Ultrasonic Array Imaging*. PhD thesis, Uppsala University, 2004.
- [7] K. Mayer, M. Ibrahim, M. Krause, M. Schubert. Requirements for a Small Size Ultrasonic Imaging System for Inspection of Concrete Elements. 2016. 19th World Conference on Non-Destructive Testing.
- [8] F. Krieg, S. Koder, J. Kirchhof, F. Römer, A. Ihlow, S. Lugin, A. Osman, and G. Del Galdo. 3D reconstruction of handheld data by SAFT and its impediment by measurement inaccuracies. In *IEEE IUS*, 2019.
- [9] R. Demirli and J. Saniie. Asymmetric Gaussian Chirplet Model for Ultrasonic Echo Analysis. *IEEE International Ultrasonics Symposium Proceedings*, 2010.
- [10] J. Kirchhof, F. Krieg, F. Römer, A. Ihlow, A. Osman, and G. Del Galdo. Speeding up 3D SAFT for ultrasonic NDT by sparse deconvolution. In *IEEE IUS*, 2016.
- [11] I. Markovsky and S. Van Huffel. Overview of total least-squares methods. *Signal Processing*, 87(10):2283 – 2302, 2007. Special Section: Total Least Squares and Errors-in-Variables Modeling.
- [12] S. Van Huffel, I. Markovsky, R. J. Vaccaro, and T. Söderström. Total least squares and errors-in-variables modeling. *Signal Processing*, 87(10):2281 – 2282, 2007.
- [13] J. Nocedal and S. J. Wright. *Numerical Optimization*. Springer-Verlag New York, 2006.
- [14] J.F. Bonnans, J. C. Gilbert, and C. Lemaréchal. C. A. Sagastizábal. *Numerical Optimization Theoretical and Practical Aspects*. Springer-Verlag Berlin Heidelberg, 2006.
- [15] NDT Engineering Corporation. *Olympus Product Catalog*. <http://www.ndt-td.ru/doc/File/ndteng.pdf>.
- [16] C. Holmes, B.W. Drinkwater, and P.D. Wilcox. Post-processing of the full matrix of ultrasonic transmit-receive array data for non-destructive evaluation. *NDT and E International*, 12 2005.
- [17] A. Rodriguez-Molares, O. M. H. Rindal, J. Dhooze, S. Måsøy, A. Austeng, M. A. L. Bell, and H. Torp. The generalized contrast-to-noise ratio: a formal definition for lesion detectability. *IEEE Transactions on Ultrasonics, Ferroelectrics, and Frequency Control*, 2019.